DALHOUSIE UNIVERSITY

Non-Covalent Interactions in Molecular Crystals: Exploring the Accuracy of the Exchange-Hole Dipole Moment Model with Local Orbitals

Luc M. LeBlanc,*,† Joseph A. Weatherby,† Alberto Otero-de-la-Roza,*,‡ and Erin R. Johnson*,†

†*Department of Chemistry, Dalhousie University, 6274 Coburg Rd, Halifax, Nova Scotia, B3H 4R2, Canada*

‡*Faculty of Chemistry, Universidad de Oviedo, 8 Avenida Julián Claveria, 33006, Oviedo, Asturias, Spain*

E-mail: luc.leblanc@dal.ca; aoterodelaroza@fluor.quimica.uniovi.es; erin.johnson@dal.ca

1 Abstract

We present the first implementation of the exchange-hole dipole moment (XDM) model in combination with a numerical finite-support local orbital method (the SIESTA method) for the modeling of non-covalent interactions in periodic solids. The XDM model is parameterised for both the B86bPBE and PBE functionals, using double-ζ- and triple-ζ-quality basis sets (DZP and TZP). The use of finite-support local orbitals is shown to have minimal impact on the computed dispersion coefficients for van-der-Waals-bound molecular dimers and small molecular solids. However, the quality of the basis set affects quite significantly the accuracy of calculated dimer binding energies and molecular crystal lattice energies; the size of the counterpoise correction indicates that this is caused by basis-set incompleteness

error. In the case of the DZP basis set, its performance for weakly bound gas-phase dimers is similar to a double-ζ Gaussian basis set without diffuse functions. The new XDM implementation was tested on graphite and phosphorene exfoliation, and on the X23 benchmark set of molecular-crystal lattice energies. Our results indicate that lattice energies similar to plane-wave calculations can be obtained only if the counterpoise correction is applied. Alternatively, the calculated equilibrium geometries are reasonably close to the plane-wave equivalents, and composite approaches in which a single-point plane-wave calculation is used at the XDM/DZP equilibrium geometry yield good accuracy at a significantly lower computational cost.

2 Introduction

The treatment of London dispersion forces[1] is crucial for the description of intermolecular interactions in materials and solids. Weak dispersion forces play an important role in determining the structural and physical properties of systems such as 2D materials[2,3] and molecular crystals.[4,5] There have been longstanding efforts to develop methods capable of modeling dispersion interactions accurately, especially in the field of density-functional theory (DFT).[6–9] While satisfactory accuracy can often be obtained with several dispersion-corrected DFT methods, it is interesting to develop computationally inexpensive variants of these methods for purposes such as *ab initio* molecular dynamics simulations or crystal structure prediction.[10–14]

One way of reducing the computational cost of a dispersion-corrected DFT method is by representing the Kohn-Sham orbitals in a basis set that ensures asymptotic linear scaling with system size as in, for example, the SIESTA method.[15,16] In SIESTA, linear scaling is achieved through a combination of $\mathcal{O}(N)$ algorithms and basis sets composed of finitely supported atom-centered numerical orbitals.[17–19] The SIESTA method is implemented in the program of the same name,[15,16] whose fourth major version release allows the treatment

of London dispersion interactions. Two dispersion methods are currently implemented in SIESTA: Grimme's semiempirical dispersion model (DFT-D2)[20,21] and the non-local van-der-Waals density functionals developed by Langreth and co-workers (vdW-DF1[22] and vdW-DF2[23]). DFT-D2 uses an asymptotic energy expression with fixed empirical dispersion coefficients; it is cheap and relatively accurate, but the coefficients are empirical and do not change with the chemical environment, which is essential in certain systems.[24] The vdW-DF methods incorporate dispersion effects using a non-local correlation energy functional. Non-local vdW-DF functionals are non-empirical and "seamless", but their use increases the computational cost significantly.[6]

An alternative approach to include dispersion effects is the exchange-hole dipole moment (XDM) dispersion model.[7,25] In XDM, the interatomic dispersion coefficients are calculated from first principles using the self-consistent density and kinetic-energy density. This makes the dispersion coefficients sensitive to the chemical environment and non-empirical, while retaining the computational and conceptual simplicity of an asymptotic, pairwise dispersion expansion. The XDM model has previously been implemented in the Quantum ESPRESSO (QE) solid-state code, which makes use of plane-wave basis sets,[26,27] and it has demonstrated excellent accuracy in the treatment of non-covalent interactions in the gas phase,[28,29] as well as for surfaces,[24] layered materials,[30,31] and molecular crystals.[14,27]

In this work, we present the first implementation of the XDM dispersion model in combination with a finite-support local-orbital method for periodic solids, as implemented in SIESTA. The resulting XDM implementation is then parameterised on the Kannemann-Becke set of molecular dimers,[32] and tested on solid-state systems such as graphite and phosphorene exfoliation, and the X23 set of molecular solids.[27,33] The implications of using local basis sets in SIESTA as opposed to delocalised plane-waves for the treatment of non-covalent interactions are discussed.

3 The XDM dispersion model: implementation, parameterisation, and testing

3.1 Theory and implementation details

The XDM dispersion model supplements the total DFT energy with a dispersion energy term:

$$E = E_{\mathrm{DFT}} + E_{\mathrm{disp}} = E_{\mathrm{DFT}} - \frac{1}{2}\sum_{\mathbf{L}}\sum_{ij}{}'\sum_{n}\frac{C_{ij}^{n} f(R_{ij\mathbf{L}})}{R_{ij\mathbf{L}}^{n}}, \tag{1}$$

where C_{ij}^{n} are the n-th order interatomic dispersion coefficients, $f(R_{ij\mathbf{L}})$ is a damping function that deactivates the dispersion interaction at short range, and

$$R_{ij\mathbf{L}} = |\mathbf{R_j} - \mathbf{R_i} + \mathbf{L}| \tag{2}$$

is the distance between atom i and j in cells separated by lattice vector $\mathbf{L}$. The prime indicates that, for $\mathbf{L} = \mathbf{0}$, i cannot equal j. In practice, the sum over lattice vectors is truncated at a point such that all remaining interatomic contributions to the total dispersion energy fall below a specified energy threshold. The Becke-Johnson damping function[7,34] has the form

$$f(R_{ij\mathbf{L}}) = \frac{1}{R_{\mathrm{vdW},ij}^{n} + R_{ij\mathbf{L}}^{n}}, \tag{3}$$

where

$$R_{\mathrm{vdW},ij} = a_1 R_{c,ij} + a_2, \tag{4}$$

$$R_{c,ij} = \frac{1}{3}\left[\left(\frac{C_{8,ij}}{C_{6,ij}}\right)^{1/2} + \left(\frac{C_{10,ij}}{C_{6,ij}}\right)^{1/4} + \left(\frac{C_{10,ij}}{C_{8,ij}}\right)^{1/2}\right]. \tag{5}$$

The sum of van der Waals radii ($R_{\mathrm{vdW},ij}$) is constructed from a critical radius, $R_{c,ij}$, corresponding to the point where dispersion contributions from the first three leading-order pairwise dispersion coefficients, C_{ij}^{6}, C_{ij}^{8}, and C_{ij}^{10}, are equal. The a_1 and a_2 parameters are

found by minimising the residual errors between computed and reference binding energies for a benchmark set of non-covalently bound dimers (the Kannemann-Becke set[32]). These parameters depend on the functional and they serve to match the long-range dispersion and short-range exchange-correlation contributions.

The XDM dispersion coefficients are determined using second-order perturbation theory.[7,25,35] Dispersion forces are calculated as interactions between instantaneous atomic multipole moments, which originate from the distribution of electron plus exchange hole dipoles.[25] The first three leading-order pairwise dispersion coefficients are

$$C_6 = \frac{\alpha_i \alpha_j \langle M_1^2 \rangle_i \langle M_1^2 \rangle_j}{\langle M_1^2 \rangle_i \alpha_j \langle M_1^2 \rangle_j \alpha_i}, \tag{6}$$

$$C_8 = \frac{3}{2} \frac{\alpha_i \alpha_j \left(\langle M_1^2 \rangle_i \langle M_2^2 \rangle_j + \langle M_2^2 \rangle_i \langle M_1^2 \rangle_j \right)}{\langle M_1^2 \rangle_i \alpha_j \langle M_1^2 \rangle_j \alpha_i}, \tag{7}$$

$$C_{10} = 2 \frac{\alpha_i \alpha_j \left(\langle M_1^2 \rangle_i \langle M_3^2 \rangle_j + \langle M_3^2 \rangle_i \langle M_1^2 \rangle_j \right)}{\langle M_1^2 \rangle_i \alpha_j \langle M_1^2 \rangle_j \alpha_i} + \frac{21}{5} \frac{\alpha_i \alpha_j \langle M_2^2 \rangle_i \langle M_2^2 \rangle_j}{\langle M_1^2 \rangle_i \alpha_j \langle M_1^2 \rangle_j \alpha_i}. \tag{8}$$

Combined, the three dispersion energy terms corresponding to the these coefficients have been shown to describe long-range interactions in solids accurately.[7,27] Thus, in the canonical XDM implementation, the summation over n in Eq. 1 is truncated at the $n = 10$ term, and only takes into consideration atomic-pairwise contributions (i.e., $n = 6, 8, 10$). Nevertheless, it is important to note that the XDM dispersion model does take into account electronic many-body effects to all orders by way of the construction of the dispersion coefficients from the exchange hole, which is evaluated using the fully-interacting electron density.

In order to compute the XDM dispersion coefficients (Eqs. 6-8), the l-th order exchange-hole multipole moments, M_l ($l = 1, 2, 3, ...$), and the atomic polarisabilities, α_i, are needed:

$$\langle M_l^2 \rangle_i = \sum_\sigma \int \omega_i(\mathbf{r}) \rho_\sigma^{\mathrm{ae}}(\mathbf{r}) \left[r_i^l - (r_i - d_{X\sigma}(\mathbf{r}))^l \right]^2 \mathrm{d}\mathbf{r}, \tag{9}$$

$$\alpha_i = \frac{\int r^3 \omega_i(\mathbf{r}) \rho_\sigma^{\mathrm{ae}}(\mathbf{r}) \mathrm{d}\mathbf{r}}{\int r^3 \rho_i^{\mathrm{at}}(\mathbf{r}) \mathrm{d}\mathbf{r}} \alpha_i^{\mathrm{at}}. \tag{10}$$

Here, $\rho_\sigma^{\rm ae}$ is the all-electron spin-density and r is the distance to atom i. The $\rho_{i,\rm at}$ and $\alpha_i^{\rm at}$ are the reference free-atom densities and polarisabilities, and ω_i is the weight of that atom's contribution to the spin-density. The weights can, in principle, be constructed using any partitioning method. In XDM, we use the Hirshfeld partitioning scheme:[36,37]

$$\omega_i(\mathbf{r}) = \frac{\rho_i^{\rm at}(\mathbf{r})}{\sum_j \rho_j^{\rm at}(\mathbf{r})}, \tag{11}$$

which is relatively simple to implement. The atomic polarisabilities (Eq. 10) are calculated from their *in vacuo* (free) counterparts ($\alpha_i^{\rm at}$) by exploiting their proportionality with the atomic volumes.[38] The in-the-solid and free atomic volumes are the numerator and denominator in Eq. 10, respectively. The all-electron spin-density, $\rho_\sigma^{\rm ae}$, is approximated from the valence spin-density by adding the core electron density.

In Eq. 9, $d_{X\sigma}$ is the dipole moment between the electron at the reference point $\mathbf{r}$ and its associated exchange-hole ($h_{X\sigma}$) given by

$$d_{X\sigma}(\mathbf{r}) = \int \mathbf{r}' h_{X\sigma}(\mathbf{r}, \mathbf{r}') \mathrm{d}\mathbf{r}' - \mathbf{r}. \tag{12}$$

The exact expression for $h_{X\sigma}$ is computationally prohibitive in solids because it involves a double sum over occupied states. Instead, we use the Becke-Roussel (BR) semi-local model for the spherically averaged exchange hole.[39] The BR hole provides a better approximation to the full exchange-correlation hole than $h_{X\sigma}$ and, consequently, it results in improved performance of the resulting dispersion-corrected energies.[7,40]

The BR model hole has the form of an off-centered exponential function ($-Ae^{-ar}$) displaced from the electron's reference point by a distance b.[27] The three parameters (A, a, b) are determined by enforcing three exact constraints related to the hole normalisation and its

value and curvature at the reference point. This leads to $b = d_{X\sigma}$, where b is calculated as

$$b^3 = \frac{x^3 e^{-x}}{8\pi\rho_\sigma^{\mathrm{val}}}, \tag{13}$$

where $x = ab$ is the solution to the non-linear equation

$$\frac{xe^{-2x/3}}{x-2} = \frac{2}{3}\pi^{2/3}\frac{{\rho_\sigma^{\mathrm{val}}}^{5/3}}{Q_\sigma}, \tag{14}$$

which is solved numerically using Newton's method. The hole curvature (Q_σ) is

$$Q_\sigma = \frac{1}{6}(\nabla^2\rho_\sigma^{\mathrm{val}} - 2D_\sigma), \tag{15}$$

with

$$D_\sigma = \tau_\sigma - \frac{1}{4}\frac{|\nabla\rho_\sigma^{\mathrm{val}}|^2}{\rho_\sigma^{\mathrm{val}}}, \tag{16}$$

where τ_σ is the positive-definite valence spin kinetic-energy density,

$$\tau_\sigma = \sum_i |\nabla\psi_{i\sigma}|^2 . \tag{17}$$

It is important to ensure that the calculated value of b does not unphysically overshoot the distance to the closest nucleus.[25,27] For this reason, $d_{X\sigma}$ is set to $\min(b, r_i)$, instead of simply b, in Eq. 9.

The XDM equations (Eq. 1 to 17) are straightforward to implement in SIESTA. In contrast to the plane-wave (QE) implementation,[26] the electron density and kinetic energy density are written as a sum over local orbitals:

$$\rho_\sigma^{\mathrm{val}} = \sum_i |\psi_{i,\sigma}|^2 = \sum_i \left|\sum_{\mu,\nu} c_{\mu,\nu}\phi_\mu\phi_\nu\right| \tag{18}$$

and

$$\tau_\sigma = \sum_i |\nabla \psi_{i,\sigma}|^2 = \sum_i \left| \sum_{\mu,\nu} c_{\mu,\nu} \left(\nabla \phi_\mu \phi_\nu + \phi_\mu \nabla \phi_\nu \right) \right|^2 , \tag{19}$$

where the $c_{\mu,\nu}$ are the density matrix elements. The sum extends only over the atomic orbitals, ϕ_μ and ϕ_ν, that give a non-zero contribution at the reference point. The moments and volumes are integrated via summation over a uniform grid.

The value of b is calculated at every point on the integration grid from the corresponding values for the valence spin density ($\rho_\sigma^{\mathrm{val}}$), its gradient norm ($|\nabla \rho_\sigma^{\mathrm{val}}|^2$), its Laplacian ($\nabla^2 \rho_\sigma^{\mathrm{val}}$), and the spin kinetic-energy density (τ_σ). To validate the implementation, these quantities and the resulting b parameter for argon are compared to the values obtained using the XDM implementations in Quantum ESPRESSO (plane waves),[26] and the numerical-orbital Numol program,[48] as shown in Figure 1. The SIESTA density, its derivatives, and the kinetic-energy density are in good agreement with Numol and Quantum ESPRESSO, except close to the core regions, where the three methods differ in their treatment (Numol is an all-electron code, while SIESTA and QE use different pseudopotentials). Figure 1 confirms that the use of finite-support numerical orbitals in SIESTA does not adversely affect the computed exchange-hole dipole moment values, when compared to either plane-wave or numerical-orbital implementations of XDM.

We also compared the XDM molecular dispersion coefficients calculated using SIESTA and Quantum ESPRESSO. The C_6 dispersion coefficients were calculated for the isolated molecules of the X23 lattice-energy benchmark set.[27,33] The mean percent errors obtained with the DZP and TZP finite-support basis sets were 5.6 and -4.9%, respectively, relative to the B86bPBE plane-wave calculations. Again, this indicates that the use of relatively compact, atom-centered basis functions does not strongly affect the dispersion energies calculated using the XDM method.

Lastly, from the dispersion energy expression (Eq. 1), it is possible to determine the

Figure 1: Quantities used to calculate the XDM dispersion coefficients along the internuclear coordinate in argon. (a) the valence spin density, $\rho_\sigma^{\mathrm{val}}$; (b) the Weizsaecker term, $|\nabla\rho_\sigma^{\mathrm{val}}|^2/\rho_\sigma^{\mathrm{val}}$; (c) the Laplacian of the spin density, $\nabla^2\rho_\sigma^{\mathrm{val}}$; (d) the spin kinetic-energy density, τ_σ; and (e) the exchange-hole dipole moment, $b = d_{X\sigma}$. All values are in atomic units. The SIESTA (red circles) and Quantum ESPRESSO[41] (blue boxes) calculations used an argon atom centered at the origin of a 3.760 Å cubic box, the PBE functional,[42] and only one **k**-point at Γ. Troullier-Martins[43–45] and Goedecker/Hartwigsen/Hutter/Teter[46,47] norm-conserving pseudopotentials were used, respectively. The Numol (black lines) calculations used the local density approximation (LDA) and an isolated argon dimer. The plots represent the values along the shortest argon-argon contact ($d_{\mathrm{Ar-Ar}} = 3.76$ Å).

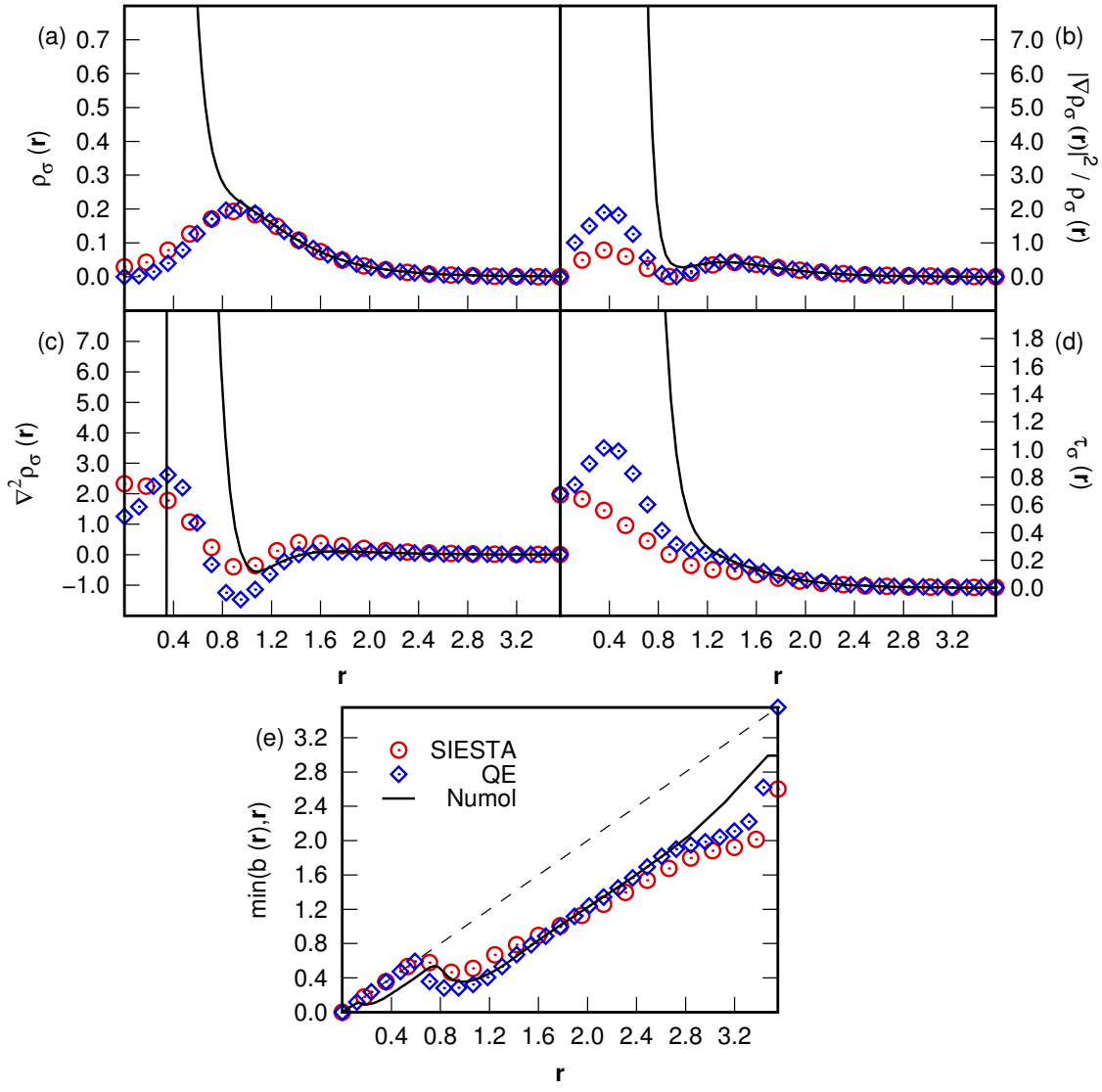

dispersion contribution to the atomic forces and the stress tensor. For atom i, the force is

$$\mathbf{F}_{\mathrm{disp},i} = \sum_{\mathbf{L}}\sum_{j}\sum_{n} \frac{nC_{n,ij}R_{ij\mathbf{L}}^{n-2}}{(R_{\mathrm{vdW},ij}^{n} + R_{ij\mathbf{L}}^{n})^2}\mathbf{R}_{\mathbf{ijL}}, \tag{20}$$

and the components of the stress tensor are

$$\sigma_{\mathrm{disp},\eta\zeta} = -\frac{1}{2V}\sum_{\mathbf{L}}\sum_{ij}{}'\sum_{n}\frac{nC_{n,ij}R_{ij\mathbf{L}}^{n-2}(R_{ij\mathbf{L}})_{\eta}(R_{ij\mathbf{L}})_{\zeta}}{(R_{\mathrm{vdW},ij}^{n}+R_{ij\mathbf{L}}^{n})^{2}}, \tag{21}$$

where $\eta, \zeta = x, y, z$ and V is the unit-cell volume. Note that, in these expressions, the dispersion coefficients are assumed to be constant with respect to changes in the crystal geometry, which is not strictly correct. However, practise has shown that this approximation does not noticeably affect the geometry minimisation, in most cases. In fact, it is more computationally efficient to calculate the dispersion coefficients at the first ionic step and then keep them constant throughout the geometry minimisation. "Relaxed" geometries are then subject to additional geometry optimisation calculations, until the newly computed dispersion coefficients, and consequently the total energy, cease to to change. The effect of fixing the dispersion coefficients at the first ionic step, as opposed to recalculating them at every step, has been tested and shown to yield equivalent geometries in both molecules and solids.

3.2 Computational Methods

SIESTA calculations: The B86bPBE[42,49] functional was implemented in our in-house version of the 4.0b-485 SIESTA code, as it typically yields the best results when paired with the XDM dispersion model.[7,26,27] Additional calculations were performed using the PBE[42] functional, with either XDM or Grimme's D2 dispersion correction.[20] Both double-ζ and triple-ζ plus polarisation (DZP and TZP) basis sets were considered. The D2 damping parameters were set to $s_r = 1.1$ and $s_6 = 0.50$ or 0.64, for DZP and TZP, respectively.[21] DZP is the standard basis set implemented in SIESTA, whereas TZP was constructed and optimised for H, N, and O atoms by Louwerse and Rothenberg,[50] and further extended to C atoms by Carter and Rohl.[51]

The confinement radius of the finite numerical orbitals was set by an "energy shift"

parameter of 0.001 Ry, found to be sufficient in reducing basis set superposition error and yielding converged energies.[14,51,52] The real-space integration grid cutoff value for charge densities and potentials was set to 200 Ry, consistent with our previous work.[14] Troullier-Martins-type[43,44] norm-conserving pseudopotentials[53,54] were generated and tested for both density functionals with the ATOM code.[45] These pseudopotentials included nonlinear core corrections.[55]

Plane-wave calculations: Reference benchmark calculations were also performed with B86bPBE-XDM, PBE-XDM, and PBE-D2 as implemented in Quantum ESPRESSO[41] v. 5.1, using plane-waves/pseudopotentials[56,57] within the projector-augmented wave (PAW) formalism.[58] The damping function parameters, a_1 and a_2, were set to 0.6512 and 1.4633 Å for B86bPBE-XDM, and to 0.3275 and 2.7673 Å for PBE-XDM.[7] The s_6 damping parameter for PBE-D2 was set to a value of 0.75. Wave-function and density cutoffs were set to 80 Ry and 800 Ry, respectively. Structure relaxations were performed with tighter thresholds for convergence of the energies and forces, i.e., 10^{-5} Ry and 10^{-4} Ry/bohr, respectively.

k-point grid sampling and structure relaxation: For all calculations, a Brillouin-zone sampling with a $4 \times 4 \times 4$ k-point Monkhorst-Pack (MP) scheme was used to treat crystal structures, whereas isolated molecules were studied at the Γ-point only. During structure optimisation, unit-cell parameters and atomic positions for crystalline systems were allowed to fully relax, while for molecules in a large-vacuum simulation box, only the atomic coordinates were allowed to vary.

Geometry relaxations were carried out using the conjugate-gradient (CG) algorithm. However, in the last stages of this study we found that the modified Broyden algorithm[59] implemented in SIESTA is much more efficient than CG, and yields the same results with tight convergence criteria (see below). Therefore, we recommend its use for geometry relaxations in molecular crystals.

Similarity index: As a tool to measure similarity between crystal structures, the POWDIFF utility in CRITIC2[60] was used. This tool is based on the comparison of powder

diffraction patterns using a cross-correlation function,[61] and ranges in value between zero and one. A result of zero indicates an exact match, while a result of one indicates maximum dissimilarity between two crystal structures.

3.3 Parameterisation of the XDM dispersion model

Table 1: XDM damping parameters for the PBE and B86bPBE functionals and selected basis sets, along with the resulting error statistics for the fit set.

Method	N^a	a_1	a_2 (Å)	MPE[b]	MAPE[c]	MAX[d]
SIESTA						
PBE/DZP	49	–	–	-17.0	39.5	232.2 (c6h6-c6h6-stack)
PBE-D2/DZP	49	–	–	20.8	33.5	130.6 (cf4-cf4)
PBE-D2/TZP	34	–	–	25.9	26.5	62.0 (ch4-nh3)
PBE-XDM/DZP	49	1.4588	0.0000[e]	14.7	30.3	132.0 (cf4-cf4)
PBE-XDM/DZP	34	1.4025	0.0000[e]	11.2	22.5	94.3 (ch4-nh3)
PBE-XDM/DZP+CP[f]	34	1.2901	0.0000[e]	-3.6	19.2	73.9 (ch4-c2h4)
PBE-XDM/TZP	34	0.7086	2.3542	1.1	**12.3**	56.0 (ch4-c2h4)
PBE-XDM/TZP+CP[f]	34	1.2480	0.0000[e]	-3.1	18.6	74.0 (ch4-c2h4)
B86bPBE/DZP	49	–	–	-32.7	43.3	158.6 (c6h6-c6h6-stack)
B86bPBE-XDM/DZP	49	0.2307	3.4210	8.7	21.7	62.4 (ch4-nh3)
B86bPBE-XDM/DZP	34	0.5000	2.5556	4.9	18.2	65.2 (ch4-nh3)
B86bPBE-XDM/DZP+CP[f]	34	1.2343	0.0000[e]	-9.7	20.4	80.4 (c6h6-ch4)
B86bPBE-XDM/TZP	34	1.3543	0.0000[e]	-1.2	**11.2**	40.4 (ch4-c2h4)
B86bPBE-XDM/TZP+CP[f]	34	1.1874	0.0000[e]	-8.4	19.2	82.7 (c6h6-ch4)
QE						
PBE-D2	49	–	–	13.2	18.4	69.7 (ch4-hf)
PBE-XDM	49	0.3275	2.7673	3.9	**13.7**	37.8 (h2s-h2s)
B86bPBE-XDM	49	0.6512	1.4633	2.6	**11.4**	23.1 (ch4-nh3)

[a] Number of molecular dimers contained in the parameterisation set. [b] Mean percent error; a negative (positive) sign indicates underbinding (overbinding) with respect to the benchmark data. [c] Mean absolute percent error. [d] Maximum absolute percent error. Labels in parentheses identify the dimer that gives the maximum error. [e] In order to avoid unphysical (negative) values, a_2 was set to zero in the fit. [f] Counterpoise corrections were applied to the computed dimer binding energies.

The XDM dispersion model was parameterised for both the (newly implemented) B86bPBE and PBE functionals by minimising residual errors with respect to high-level benchmark data from the Kannemann-Becke (KB49) set of 49 weakly bound molecular dimers.[32] Hybrid functionals, involving a fraction of exact exchange, are not currently implemented in the SIESTA code and were not considered here. In all cases, single-point energy calculations were performed at the fixed benchmark set geometries. The optimal parameters obtained by least-squares fit, and the performance of the XDM-corrected methods, are shown in Table 1 for the standard DZP basis set and the extended TZP basis set.[50,51] Because the TZP basis is not available for all elements contained in the KB49 data (namely, Si, S and F), the XDM model was parameterised on a subset of the KB set containing 34 dimers (of a total of 49,

not counting the noble gas dimers). For consistency, the parameters obtained by fitting to the 34-dimer set will be used for both the DZP and TZP basis sets in the rest of the article.

The B86bPBE average errors in Table 1 are consistently lower than those from PBE, when paired with XDM. This has been observed in previous studies,[26,28] and is expected from the large-gradient-limit behavior of the exchange enhancement factor in these functionals.[7,62,63] Using the largest basis set in this study (TZP), the MAPE of both functionals (12.3% for PBE and 11.2% for B86bPBE) are very similar to those obtained using QE (13.7% and 11.4%) and also to the near-complete-basis-set values using Gaussian basis sets reported in a previous study[28] (14.3% and 13.1% for the full KB49 set, with the latter value obtained using the psi4 program[64]). For comparison, PBE-D2 gives MAPEs of 33.5% (DZP), 26.5% (TZP), and 18.4% using the QE implementation. However, it must be noted that PBE-D2 was not specifically fitted to the KB set.

The performance of B86bPBE-XDM and PBE-XDM suffers considerably from basis set incompleteness when the smaller DZP basis set provided in the SIESTA package is used, with MAPEs of 21.7% (B86bPBE) and 30.0% (PBE), if the full KB49 set is considered. These values are consistent with the results for double-ζ Gaussian basis sets lacking diffuse functions, previously shown to be inadequate for non-covalent interactions.[28,65] For example, the MAPE of the PBE-XDM parameterisation to the 49-dimer KB set with non-diffuse double-ζ Gaussian basis sets is 37.2% (6-31G$*$) and 45.9% (cc-pVDZ). In contrast, the MAPE of 6-31+G$*$, which contains one set of diffuse functions, is 17.8%. The DZP MAPE of 30.3% is intermediate between these two results, while the TZP basis set benefits from the increased cutoff radii compared to DZP. Other functionals, such as PBE-D2, are similarly affected by basis-set incompleteness, with MAPEs of 26.5% (TZP) and 33.5% (DZP). Therefore, it is clear that reliable calculation of non-covalent binding energies in SIESTA necessitates the use of larger basis sets than the standard DZP, or the design of new basis sets with increased cutoff radii.

The use of counterpoise (CP) corrections[66] to account for basis set superposition error

(BSSE), in conjunction with the DZP or TZP basis sets, does not improve the performance of any method other than PBE-XDM/DZP. The CP correction tends to over-compensate, causing the dimers to be underbound on average, in agreement with previous reports.[67] The size of the CP correction indicates that there is still significant basis-set incompleteness error in the TZP results, probably stemming from the finite-support nature of the basis set.

3.4 Graphite and phosphorene exfoliation

We now consider the exfoliation[68] of graphite and phosphorene using the new XDM-corrected functionals in SIESTA. Graphite exfoliation is a simple test of the accuracy in the treatment of non-covalent interactions for which high-level experimental reference data exists.[69] For each method in Table 1, a scan was performed by systematically varying the interlayer distance between graphene sheets in graphite, while the intralayer hexagonal lattice parameter was kept fixed at 2.456 Å. The resulting potential energy curves are shown in Figure 2.

In all cases, the energy curves for the uncorrected functionals (PBE and B86bPBE) are very slightly binding, or non-binding, and a dispersion correction is necessary to obtain physically meaningful results. The equilibrium interlayer separations using DZP and TZP are slightly higher (≈0.1–0.2 Å) than the plane-wave results and the experimental reference data. The exfoliation energies computed with SIESTA are in close agreement with both experiment and the QE calculations, although slightly underestimated with the DZP basis set. Overall, the DFT-XDM methods perform slightly better at reproducing the experimental graphite interlayer distance and exfoliation energy than PBE-D2, regardless of the choice of local or plane-wave basis sets.

Counter-intuitively, while it is the larger basis set, TZP was found to to have increased BSSE for this system, as quantified by the greater counterpoise correction (see Supporting Information). This is due to the more diffuse nature of the TZP basis for carbon, leading to greater orbital overlap. The BSSE leads to increased interlayer binding with TZP for all functionals, relative to the plane-wave results. In particular, uncorrected B86bPBE and

Figure 2: Graphite exfoliation curves calculated with plane-wave/pseudopotentials in (a) QE, (b) SIESTA using a DZP basis set, and (c) SIESTA using a TZP basis set, compared to experimental data.[69]

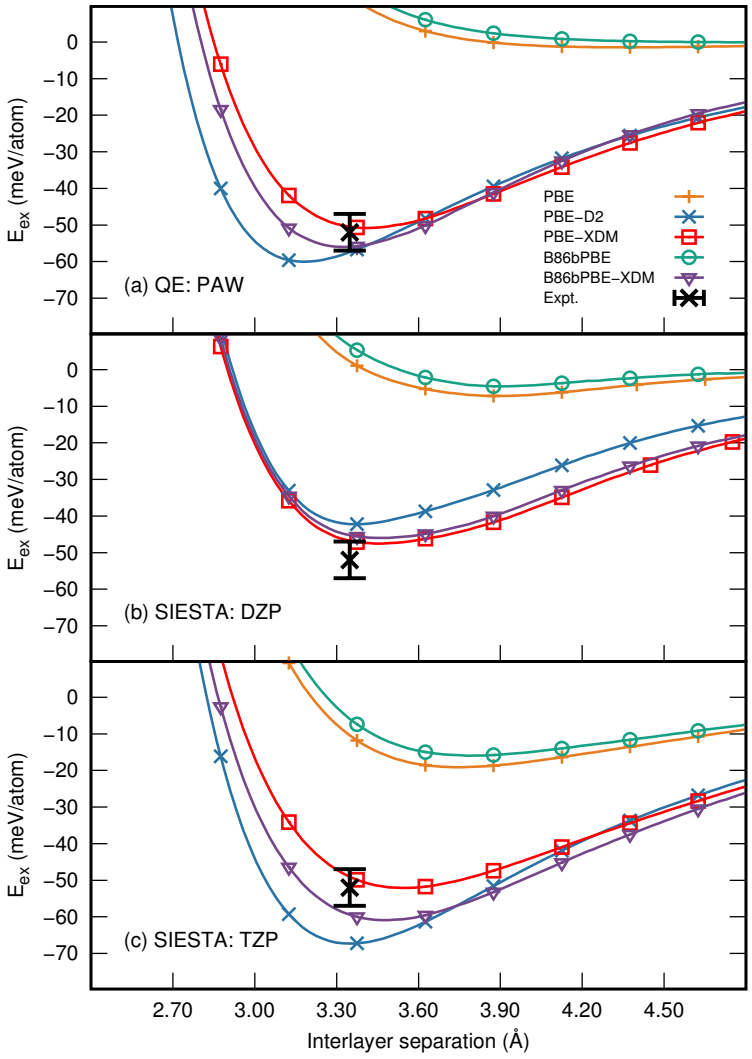

PBE show between 10–20 meV/atom of spurious binding, while they are entirely repulsive with the plane-wave basis.

Phosphorene,[70] the single- (or few-) layer black phosphorus analogue of graphite, has attracted great interest recently due to its properties for device applications, which could be superior to those of graphene.[71–74] It has also been reported to be an "extremely challenging system from a computational point of view, given that its properties are regulated by a delicate equilibrium between dispersion forces and covalent interactions".[75]

While no experimental measurement for the mechanical exfoliation of phosphorene has

been reported, many theoretical predictions have been made: quantum diffusion Monte Carlo (DMC, -81±6 meV/atom),[76] post-HF periodic wave-correlated theory (p-LMP2 and pHF with CCSD(T) corrections, -151 meV/atom and -92 meV/atom, respectively),[77,78] along with several dispersion-corrected GGA DFT computations (falling in the ca. -80 to -150 meV/atom range).[75,77]

For each method in Table 1, a similar scan to what was done for graphite exfoliation was performed for the phosphorene analogue. The interlayer distance between sheets of black phosphorus (3.108Å at equilibrium) was systematically varied, while the intralayer orthorhombic lattice parameters were kept fixed at the experimental values of 3.314Å and 4.376Å.[79] The resulting potential energy curves are shown in Figure 3.

Figure 3: Phosphorene exfoliation curves calculated with plane-wave/pseudopotentials in (a) QE, and (b) SIESTA using a DZP basis set.

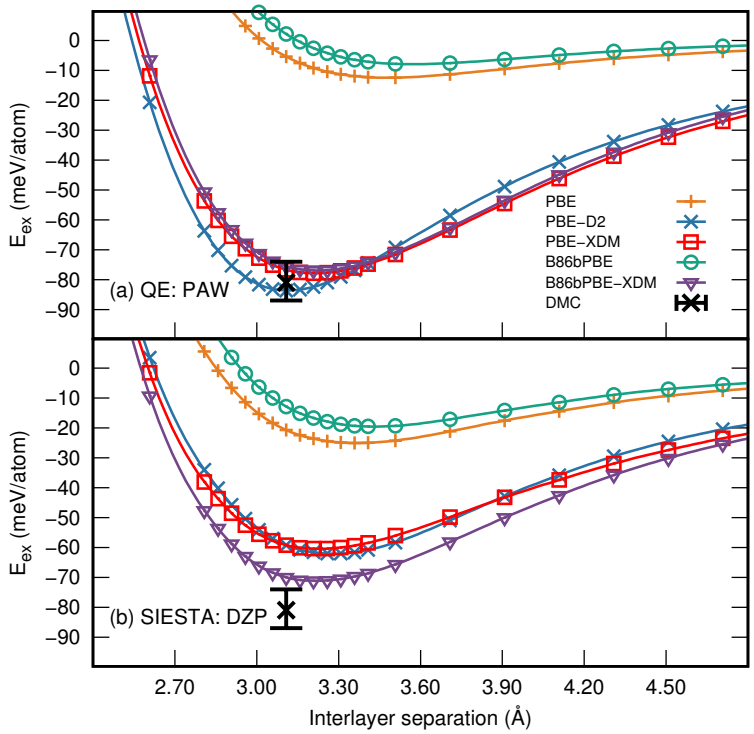

As Quantum Monte Carlo methods are often used as benchmarking tools,[80,81] we compare to the DMC result (-81±6 meV/atom) for the phosphorene exfoliation energy.[76] The curves depicted in Figure 3 clearly show that the equilibrium geometry and exfoliation energy are

well captured by both the plane-wave and numerical basis set calculations, although, as seen for graphite, the exfoliation energy is somewhat underestimated with DZP. In this instance, a TZP basis set was not available for the phosphorus atom and was not considered.

Before proceeding to the following section, there is an important point to note about geometry optimisations in weakly bound crystals using SIESTA. The default convergence thresholds for maximum atomic force and maximum stress components in SIESTA are 0.04 eV/Å and 1.0 GPa, respectively. While these are suitable for hard solids, they lead to unfinished geometry optimisations in molecular crystals, which makes the energy landscapes dependent on the choice of input geometries.[14] This is illustrated by varying maximum stress component threshold for calculations on graphite (Table 2). The default convergence threshold (1.0 GPa) leads to incomplete geometry optimisations and erroneous equilibrium geometries. From these tests and previous work,[14] maximum force and stress thresholds of 0.01 eV/Å and 0.02 GPa, which are tighter than the defaults, seem to be sufficient. These convergence thresholds will be used in the rest of the article. It is important to note that excessively tight stress thresholds are also problematic because of numerical instabilities that arise near the cutoff radii of the finite-support atomic orbitals when performing numerical integration.[15,16] This can lead to "endless" geometry optimisations, as pointed out by the SIESTA developers.

3.5 Lattice energies of molecular crystals

We now assess the SIESTA implementation of XDM for molecular crystals. The statistics on the X23 benchmark set are shown in Table 3. The X23 set[27,33] contains reference lattice energies for 23 small-molecule crystals. With the DZP basis set, B86bPBE-XDM performs best overall, yielding an MAE of 8.2 kJ/mol, followed by PBE-D2 and PBE-XDM. However, the use of the larger TZP basis set does not necessarily improve the quality of the results. Similar to Carter and Rohl,[51] we observe that the lattice-energy error statistics with finite-support basis sets are somewhat poorer than using plane waves. Carter and Rohl obtained

Table 2: Results of geometry optimisations on graphite performed with DFT-XDM/DZP and DFT-D2/DZP using various input values of the c lattice parameter (specified in parentheses), as a function of the stress convergence threshold.[a]

Stress thr.	N_{opt}	c (6.0)	N_{opt}	c (7.0)	N_{opt}	c (8.0)
B86bPBE-XDM						
1.0	21	6.939	6	6.998	31	7.315
0.02	78	6.936	58	6.937	146	6.940
0.002	126	6.936	179	6.937	248	6.937
PBE-XDM						
1.0	21	6.988	6	6.999	30	7.069
0.02	47	6.996	23	6.998	163	6.995
0.002	309	6.976	291	6.977	314	6.991
PBE-D2						
1.0	13	6.871	2	6.994	19	6.820
0.02	19	6.796	46	6.797	62	6.798
0.002	66	6.795	105	6.795	137	6.795

[a] The units are GPa for the cell stresses, and Å for the c lattice parameter. N_{opt} is the number of optimisation steps.

a MAE of ca. 23 kJ/mol on the C21 subset of X23 (with 21 lattice energies[27]) using the non-local vdW-DF methods and a DZP basis set. For comparison, plane-wave calculations with the same functionals yield MAEs of ca. 10 kJ/mol.[27] Thus, for molecular crystals, B86bPBE-XDM/DZP outperforms the vdW-DF methods,[7] even when employed with plane waves, at a considerably reduced computational cost.

Carter and Rohl also demonstrated that the application of counterpoise corrections greatly reduced the errors in the computed lattice energies with SIESTA, restoring the performance of the vdW-DF functionals to the same quality as their plane-wave implementation.[51] Upon applying CP corrections, all of the DFT-XDM methods yield MAEs of 4.4–4.7 kJ/mol, approaching those of the plane-wave reference calculations. However, as argued previously,[51] although CP corrections significantly improve lattice energies and return values similar to plane-wave calculations, they are not straightforward to apply.

The impact of basis set incompleteness error on the lattice energies in Table 3 raises the question of whether the equilibrium geometries are similarly affected. This question is also important in the context of composite methods, in which high-level single-point calculations

Table 3: Statistics for the X23 set of lattice energies using DFT-XDM and DFT-D2 methods, in kJ/mol per molecule, relative to back-corrected, experimental sublimation enthalpies.[27,33]

Method	ME[a]	MAE[b]	MAX[c]
SIESTA			
PBE-D2/DZP	7.5	11.4	25.1 (ant)
PBE-D2/TZP	3.9	5.7	14.5 (ada)
PBE-XDM/DZP	11.8	14.1	29.9 (suc)
PBE-XDM/TZP	-9.4	10.0	23.0 (cyt)
B86bPBE-XDM/DZP	3.1	8.2	24.3 (ant)
B86bPBE-XDM/TZP	-8.4	8.9	21.3 (cyt)
PBE-XDM/DZP+CP[d]	-0.8	4.4	14.4 (ant)
PBE-XDM/TZP+CP[d]	-2.1	4.4	18.2 (ant)
B86bPBE-XDM/DZP+CP[d]	-3.2	4.7	15.8 (ant)
B86bPBE-XDM/TZP+CP[d]	-3.6	4.7	17.5 (ant)
QE			
PBE-D2	3.7	5.8	18.4 (ada)
PBE-XDM	-3.2	4.7	17.9 (cyt)
B86bPBE-XDM	0.5	3.6	13.4 (cyt)
QE//SIESTA[e]			
PBE-D2/DZP	2.9	5.5	13.7 (cya)
PBE-XDM/DZP	-2.5	4.3	17.2 (cyt)
B86bPBE-XDM/DZP	-0.1	3.7	12.7 (cyt)

[a] Mean error; a negative (positive) ME indicates underbinding (overbinding) with respect to the benchmark data. [b] Mean absolute error. [c] Maximum absolute error; labels in parentheses identify the crystal responsible (ada: adamantane, ant: anthracene, cya: cyanamide, cyt: cytosine, suc: succinic acid). [d] Counterpoise corrections were applied to the crystal lattice energies, following the approach of Carter and Rohl.[51] [e] Composite methods using plane-wave single-point energies evaluated using the geometries obtained from SIESTA with the same functional and the DZP basis.

(using plane waves) are used at geometries obtained using a low-level calculation (SIESTA). Composite methods have been proposed as a computationally efficient alternative to plane waves for the calculation of lattice energies in molecular crystals,[14,51] but their performance relies on whether the low-level method offers equilibrium geometries close to those of the high-level method.

Table 4 evaluates the ability of DZP calculations with SIESTA to reproduce plane-wave equilibrium geometries, using the same density functional and dispersion correction. The plane-wave geometries are close to the complete-basis-set limit and, in our experience, the

Table 4: Statistics for the X23 set of lattice energies using composite methods, in kJ/mol per molecule, relative to plane-wave calculations with the same density functional.

	SIESTA	QE//SIESTA			
Method	MAE[a]	ME[b]	MAE[a]	MAX[c]	POWDIFF[d]
PBE-D2/DZP	10.8	-0.8	1.2	5.4 (ada)	0.2935
PBE-XDM/DZP	15.0	0.8	0.8	2.0 (pyr)	0.1578
B86bPBE-XDM/DZP	7.0	0.5	0.6	1.2 (eth)	0.1975

[a] Mean absolute error. [b] Mean error; a negative (positive) ME indicates underbinding (overbinding) with respect to the benchmark data. [c] Maximum absolute error; labels in parentheses identify the crystal responsible (ada: adamantane, eth: ethylcarbamate, pyr: pyrazole). [d] The deviation between the SIESTA and QE equilibrium geometries is quantified by the powder diffraction similarity measure.

choice of PAW dataset/pseudopotential has very little effect on non-covalent equilibrium geometries, provided enough plane waves are used in the calculation. The powder similarity measure (POWDIFF) indicates that there are significant differences between the SIESTA and plane-wave geometries, and that this deviation is somewhat smaller for XDM than for D2. However, the lattice energies calculated using the corresponding composite methods are excellent, with MAEs being within at most 1.2 kJ/mol from the pure plane-wave calculations. Therefore, even though the lattice energies calculated using the DZP basis set are significantly affected by basis-set incompleteness error (Table 3), the corresponding equilibrium geometries seem to be reasonably close to the plane-wave reference and, consequently, the composite methods built with a DFT-XDM/DZP low-level approach are quite accurate and significantly cheaper than a pure plane-wave optimisation.

4 Conclusions

In this article, we presented the first implementation of the XDM dispersion model with the numerical finite-supported orbital method in the SIESTA software package. The new SIESTA/XDM code was verified by comparing the calculated dispersion coefficients to other XDM implementations using plane waves (QE) and numerical orbitals in the gas phase (Numol). The XDM method in SIESTA was then parameterised against the Kannemann-

Becke set of gas-phase binding energies of molecular dimers for the PBE and B86bPBE functionals, with double-ζ (DZP) and triple-ζ (TZP) basis sets. DZP is the default basis set in SIESTA, while TZP has been recently formulated for C, H, O, and N by Louwerse and Rothenberg[50] and Carter and Rohl.[51] The performance of the new XDM-corrected methods for the molecular dimers is of similar quality to the results, obtained using plane waves, provided that the TZP basis set is employed. DZP, on the other hand, suffers from significant basis-set incompleteness, and its performance is similar to double-ζ Gaussian basis sets without diffuse functions.

The new XDM implementation was tested for three cases: graphite and phosphorene exfoliation, and the calculation of lattice energies of molecular crystals. The XDM dispersion correction brings the potential energy curves for graphite and phosphorene exfoliation into close agreement with experimental data (or theoretical benchmark data, in the case of phosphorene). For the molecular crystal lattice energies, the XDM-corrected SIESTA methods also give good results, although care needs to be taken in using/setting the proper stress convergence thresholds for geometry optimisations.

Both the DZP and TZP basis sets display considerable basis set incompleteness effects, causing the predicted lattice energies to be inferior to the plane-wave results unless counterpoise corrections are applied, which is undesirable in practice. This reveals the necessity of designing specialised SIESTA basis sets for non-covalent interactions. However, the equilibrium geometries obtained from all XDM-corrected methods in SIESTA are quite close to the plane-wave results. It was shown that composite approaches, in which a single-point plane-wave calculation is performed at SIESTA's DZP equilibrium geometries, are quite accurate and computationally efficient.

B86bPBE-XDM/DZP showed particular promise as an excellent balance between accuracy and efficiency when determining lattice energies. The performance of this method is a significant improvement over the currently implemented post-SCF dispersion corrections (DFT-D2) and non-local functionals (vdW-DF1 and vdW-DF2) in SIESTA. While the ap-

plications examined in this work were focused on layered materials and organic molecular crystals, there are no reasons that would impede the use of the local-orbital implementation XDM for computations on ionic or covalent bulk solids.

Acknowledgement

The authors acknowledge the Natural Sciences and Engineering Research Council of Canada (NSERC) for financial support and Compute Canada (ACEnet and Westgrid) for computational resources. L.M.L. would also like to acknowledge the Walter C. Sumner Foundation for financial support. The authors would like to further thank Dr. Ross Dickson, Computational Research Consultant for ACEnet, for invaluable discussions concerning the MPI-parallelisation of the XDM model within SIESTA.

Supporting Information Available

Computed and benchmark binding energies for the KB49 set of molecular dimers and lattice energies for the X23 set crystal structures. Tests for basis set superposition errors in graphene exfoliation. This material is available free of charge via the Internet at `http://pubs.acs.org/`.

References

(1) Otero-de-la-Roza, A.; DiLabio, G. *Non-Covalent Interactions in Quantum Chemistry and Physics*; Elsevier: Amsterdam, Netherlands, 2017.

(2) Lorenzo, A.; Escribano, B.; Akhmatskaya, E.; Carrasco, J. Assessment of van der Waals Inclusive Density Functional Theory Methods for Layered Electroactive Materials. *Phys. Chem. Chem. Phys.* **2017**, *19*, 10133–10139.

(3) Tawfik, S. A.; Gould, T.; Stampfl, C.; Ford, M. J. Evaluation of van der Waals Density Functionals for Layered Materials. *Phys. Rev. Materials* **2018**, *2*, 034005.

(4) Reilly, A. M.; Cooper, R. I.; Adjiman, C. S.; Bhattacharya, S.; Boese, A. D.; Brandenburg, J. G.; Bygrave, P. J.; Bylsma, R.; Campbell, J. E.; Car, R.; Case, D. H.; Chadha, R.; Cole, J. C.; Cosburn, K.; Cuppen, H. M.; Curtis, F.; Day, G. M.; DiStasio Jr, R. A.; Dzyabchenko, A.; van Eijck, B. P.; Elking, D. M.; van den Ende, J. A.; Facelli, J. C.; Ferraro, M. B.; Fusti-Molnar, L.; Gatsiou, C.-A.; Gee, T. S.; de Gelder, R.; Ghiringhelli, L. M.; Goto, H.; Grimme, S.; Guo, R.; Hofmann, D. W. M.; Hoja, J.; Hylton, R. K.; Iuzzolino, L.; Janckiewicz, W.; de Jong, D. T.; Kendrick, J.; de Klerk, N.; Ko, H.-Y.; Kuleshova, L. N.; Li, X.; Lohani, S.; Leusen, F.; Lund, A. M.; Lv, J.; Ma, Y.; Marom, N.; Masunov, A. E.; McCabe, P.; McMahon, D. P.; Meekes, H.; Metz, M. P.; Misquitta, A. J.; Mohamed, S.; Monserrat, B.; Needs, R. J.; Neumann, M. A.; Nyman, J.; Obata, S.; Oberhofer, H.; Oganov, A. R.; Orendt, A. M.; Pagola, G. I.; Pantelides, C. C.; Pickard, C. J.; Podeszwa, R.; Price, L. S.; Price, S. L.; Pulido, A.; Read, M. G.; Reuter, K.; Schneider, E.; Schober, C.; Shields, G. P.; Singh, P.; Sugden, I. J.; Szalewicz, K.; Taylor, C. R.; Tkatchenko, A.; Tuckerman, M. E.; Vacarro, F.; Vasileiadis, M.; Vazquez-Mayagoitia, A.; Vogt, L.; Wang, Y.; Watson, R. E.; de Wijs, G. A.; Yang, J. Z.; Zhu, Q.; Groom, C. R. Report on the Sixth Blind Test of Organic Crystal-Structure Prediction Methods. *Acta Crystallogr., Sect. B: Struct. Sci.* **2016**, *72*, 439–459.

(5) Beran, G. Modelling Polymorphic Molecular Crystals with Electronic Structure Theory. *Chem. Rev.* **2016**, *116*, 5567–5613.

(6) Grimme, S. Dispersion-Corrected Mean-Field Electronic Structure Methods. *Chem. Rev.* **2016**, *116*, 5105–5154.

(7) Johnson, E. R. In *Non-Covalent Interactions in Quantum Chemistry and Physics*;

Otero-de-la-Roza, A., DiLabio, G., Eds.; Elsevier: Amsterdam, Netherlands, 2017; Chapter 5, pp 169–192.

(8) Hermann, J.; DiStasio Jr., R. A.; Tkatchenko, A. First-Principles Models for van der Waals Interactions in Molecules and Materials: Concepts, Theory, and Applications. *Chem. Rev.* **2017**, *117*, 4714–4758.

(9) Berland, K.; Cooper, V. R.; Lee, K.; Schröder, E.; Thonhauser, T.; Hyldgaard, P.; Lundqvist, B. I. van der Waals Forces in Density Functional Theory: A Review of the vdW-DF Method. *Rep. Prog. Phys.* **2015**, *78*, 066501.

(10) Caldeweyher, E.; Bannwarth, C.; Grimme, S. Extension of the D3 Dispersion Coefficient Model. *J. Chem. Phys.* **2017**, *147*, 034112.

(11) Tao, J.; Zheng, F.; Gebhardt, J.; Perdew, J. P.; Rappe, A. M. Screened van der Waals Correction to Density Functional Theory for Solids. *Phys. Rev. Materials* **2017**, *1*, 020802(R).

(12) Caldeweyher, E.; Brandenburg, J. G. Simplified DFT Methods for Consistent Structures and Energies of Large Systems. *J. Phys.: Condens. Matter* **2018**, *30*, 213001.

(13) Dolgonos, G. A.; Loboda, O. A.; Boese, A. D. Development of Embedded and Performance of Density Functional Methods for Molecular Crystals. *J. Phys. Chem. A* **2018**, *122*, 708–713.

(14) LeBlanc, L. M.; Otero-de-la-Roza, A.; Johnson, E. R. Composite and Low-Cost Approaches for Molecular Crystal Structure Prediction. *J. Chem. Theory Comput.* **2018**, *14*, 2265–2276.

(15) Soler, J. M.; Artacho, E.; Gale, J. D.; García, A.; Junquera, J.; Ordejón, P.; Sánchez-Portal, D. The SIESTA Method for *Ab Initio* Order-*N* Materials Simulation. *J. Phys.: Condens. Matter* **2002**, *14*, 2745–2779.

(16) Artacho, E.; Gale, J. D.; García, A.; Junquera, J.; Martin, R. M.; Ordejón, P.; Pruneda, J. M.; Sánchez-Portal, D.; Soler, J. M. The SIESTA Method; Developments and Applicability. *J. Phys.: Condens. Matter* **2008**, *20*, 064208.

(17) Sánchez-Portal, D.; Ordejón, P.; Artacho, E.; Soler, J. M. Density-Functional Method for Very Large Systems with LCAO Basis Sets. *Int. J. Quantum Chem.* **1997**, *65*, 453–461.

(18) Artacho, E.; Sánchez-Portal, D.; Ordejón, P.; García, A.; Soler, J. M. Linear-Scaling ab-initio Calculations for Large and Complex Systems. *Phys. Stat. Sol.* **1999**, *215*, 809–817.

(19) Junquera, J.; Paz, O.; Sánchez-Portal, D.; Artacho, E. Numerical Atomic Orbitals for Linear-Scaling Calculations. *Phys. Rev. B* **2001**, *64*, 235111.

(20) Grimme, S. Semiempirical GGA-Type Density Functional Constructed with a Long-Range Dispersion Correction. *J. Comput. Chem.* **2006**, *27*, 1787–1799.

(21) Peverati, R.; Baldridge, K. K. Implementation and Performance of DFT-D with Respect to Basis Set and Functional for Study of Dispersion Interactions in Nanoscale Aromatic Hydrocarbons. *J. Chem. Theory. Comput.* **2008**, *4*, 2030–2048.

(22) Dion, M.; Rydberg, H.; Schröder, E.; Langreth, D. C.; Lundqvist, B. I. Van der Waals Density Functional for General Geometries. *Phys. Rev. Lett.* **2004**, *92*, 246401.

(23) Lee, K.; Murray, E. D.; Kong, L.; Lundqvist, B. I.; Langreth, D. C. Higher-Accuracy van der Waals Density Functional. *Phys. Rev. B* **2010**, *82*, 081101.

(24) Christian, M. S.; Otero-de-la-Roza, A.; Johnson, E. R. Surface Adsorption from the Exchange-Hole Dipole Moment Dispersion Model. *J. Chem. Theory Comput.* **2016**, *12*, 3305–3315.

(25) Becke, A. D.; Johnson, E. R. Exchange-hole Dipole Moment and the Dispersion Interaction Revisited. *J.Chem. Phys.* **2007**, *127*, 154108.

(26) Otero-de-la-Roza, A.; Johnson, E. R. Van der Waals Interactions in Solids Using the Exchange-Hole Dipole Moment Model. *J. Chem. Phys.* **2012**, *136*, 174109.

(27) Otero-de-la-Roza, A.; Johnson, E. R. A Benchmark for Non-Covalent Interactions in Solids. *J. Chem. Phys.* **2012**, *137*, 054103.

(28) Otero-de-la-Roza, A.; Johnson, E. R. Non-Covalent Interactions and Thermochemistry using XDM-Corrected Hybrid and Range-Separated Hybrid Density Functionals. *J. Chem. Phys.* **2013**, *138*, 204109.

(29) Otero-de-la-Roza, A.; Johnson, E. R. Predicting Energetics of Supramolecular Systems Using the XDM Dispersion Model. *J. Chem. Theory Comput.* **2015**, *11*, 4033–4040.

(30) Christian, M. S.; Otero-de-la-Roza, A.; Johnson, E. R. Adsorption of Graphene to Nickel (111) Using the Exchange-Hole Dipole Moment Model. *Carbon* **2017**, *118*, 184–191.

(31) Christian, M. S.; Otero-de-la-Roza, A.; Johnson, E. R. Adsorption of Graphene to Metal (111) Surfaces Using the Exchange-Hole Dipole Moment Model. *Carbon* **2017**, *124*, 531–540.

(32) Kannemann, F. O.; Becke, A. D. van der Waals Interactions in Density-Functional Theory: Intermolecular Complexes. *J. Chem. Theory Comput.* **2010**, *6*, 1081–1088.

(33) Reilly, A. M.; Tkatchenko, A. Understanding the Role of Vibrations, Exact Exchange, and Many-Body van der Waals Interactions in the Cohesive Properties of Molecular Crystals. *J. Chem. Phys.* **2013**, *139*, 024705.

(34) Johnson, E. R.; Becke, A. D. A Post-Hartree-Fock Model of Intermolecular Interactions: Inclusion of Higher-Order Corrections. *J. Chem. Phys.* **2006**, *124*, 174104.

(35) Salem, L. The Calculation of Dispersion Forces. *Mol. Phys.* **1960**, *3*, 441–452.

(36) Hirshfeld, F. L. Bonded-Atom Fragments for Describing Molecular Charge Densities. *Theoret. Chim. Acta* **1997**, *44*, 129–138.

(37) Heidar-Zadeh, F.; Ayers, P. W.; Verstraelen, T.; Vinogradov, I.; Vöhringer-Martinez, E.; Bultinck, P. Information-Theoretic Approaches to Atoms-in-Molecules: Hirshfeld Family of Partioning Schemes. *J. Phys. Chem. A* **2018**, *122*, 4219–4245.

(38) Kannemann, F. O.; Becke, A. D. Atomic Volumes and Polarizabilities in Density-Functional Theory. *J. Chem. Phys.* **2012**, *136*, 034109.

(39) Becke, A. D.; Roussel, M. R. Exchange Holes in Inhomogeneous Systems: A Coordinate Space Model. *Phys. Rev. A* **1989**, *39*, 3761–3767.

(40) Becke, A. D.; Johnson, E. R. A Density-Functional Model of the Dispersion Interaction. *J. Chem. Phys.* **2005**, *123*, 154101.

(41) Giannozzi, P.; Andreussi, O.; Brumme, T.; Bunau, O.; Buongiorno Nardelli, M.; Calandra, M.; Car, R.; Cavazzoni, C.; Ceresoli, D.; Cococcioni, M.; Colonna, N.; Carnimeo, I.; Dal Corso, A.; de Gironcoli, S.; Delugas, P.; DiStasio, R.; Ferretti, A.; Floris, A.; Fratesi, G.; Fugallo, G.; Gebauer, R.; Gerstmann, U.; Giustino, F.; Gorni, T.; Jia, J.; Kawamura, M.; Ko, H.-Y.; Kokalj, A.; Küçükbenli, E.; Lazzeri, M.; Marsili, M.; Marzari, N.; Mauri, F.; Nguyen, N. L.; Nguyen, H.-V.; Otero-de-la-Roza, A.; Paulatto, L.; Poncé, S.; Rocca, D.; Sabatini, R.; Santra, B.; Schlipf, M.; Seitsonen, A.; Smogunov, A.; Timrov, I.; Thonhauser, T.; Umari, P.; Vast, N.; Baroni, S. Advanced Capabilities for Materials Modelling with Quantum ESPRESSO. *J. Phys.: Condens. Matter* **2017**, *29*, 465901.

(42) Perdew, J. P.; Burke, K.; Ernzerhof, M. Generalized Gradient Approximation Made Simple. *Phys. Rev. Lett.* **1996**, *77*, 3865–3868.

(43) Troullier, N.; Martins, J. L. Efficient Pseudopotentials for Plane-Wave Calculations. *Phys. Rev. B* **1991**, *43*, 1993–2006.

(44) Troullier, N.; Martins, J. L. Efficient Pseudopotentials for Plane-Wave Calculations. II. Operators for Fast Iterative Diagonalization. *Phys. Rev. B* **1991**, *43*, 8861–8869.

(45) *ATOM, a program for DFT calculations in atoms and pseudopotential generation, maintained by Alberto Garcia and distributed as part of the SIESTA package. See* `http://www.icmab.es/siesta/atom`

(46) Goedecker, S.; Teter, M.; Hutter, J. Separable Dual-Space Gaussian Pseudopotentials. *Phys. Rev. B* **1996**, *54*, 1703–1710.

(47) Hartwigsen, C.; Goedecker, S.; Hutter, J. Relativistic Separable Dual-Space Gaussian Pseudopotentials from H to Rn. *Phys. Rev. B* **1998**, *58*, 3641–3662.

(48) Becke, A. D.; Dickson, R. M. Numerical-Solution of Schrodinger-Equation in Polyatomic-Molecules. *J. Chem. Phys.* **1990**, *92*, 3610–3612.

(49) Becke, A. D. On the Large-Gradient Behavior of the Density Functional Exchange Energy. *J. Chem. Phys.* **1986**, *85*, 7184–7187.

(50) Louwerse, M. J.; Rothenberg, G. Transferrable Basis Sets of Numerical Atomic Orbitals. *Phys. Rev. B* **2012**, *85*, 035108.

(51) Carter, D. J.; Rohl, A. L. Benchmarking Calculated Lattice Parameters and Energies of Molecular Crystals Using van der Waals Density Functional. *J. Chem. Theory Comput.* **2014**, *10*, 3423–3437.

(52) Chapman, C.; Ting, E. C.; Kereszti, A.; Paci, I. Self-Assembly of Cysteine Dimers at the Gold Surface: A Computational Study of Competing Interactions. *J. Phys. Chem. C* **2013**, *117*, 19426–19435.

(53) Hamann, D. R.; Schlüter, M.; Chiang, C. Norm-Conserving Pseudopotentials. *Phys. Rev. Lett.* **1979**, *43*, 1494–1497.

(54) Bachelet, G. B.; Hamann, D. R.; Schlüter, M. Pseudopotentials That Work: From H to Pu. *Phys. Rev. B* **1982**, *26*, 4199–4228.

(55) Louie, S. G.; Froyen, S.; Cohen, M. L. Nonlinear Ionic Pseudopotentials in Spin-Density-Functional Calculations. *Phys. Rev. B* **1982**, *26*, 1738–1742.

(56) Pickett, W. E. Pseudopotential Methods in Condensed Matter Applications. *Comput. Phys. Rep.* **1989**, *9*, 115–197.

(57) Payne, M. C.; Teter, M. P.; Allan, D. C.; Arias, T. A.; Joannopoulos, J. D. Iterative Minimzation Techniques for Ab Initio Total-Energy Calculations: Molecular Dynamics and Conjugate Gradients. *Rev. Mod. Phys.* **1992**, *64*, 1045–1097.

(58) Blöchl, P. E. Projector Augmented-Wave Method. *Phys. Rev. B* **1994**, *50*, 17953–17979.

(59) Johnson, D. D. Modified Broyden's Method for Accelerating Convergence in Self-Consistent Calculations. *Phys. Rev. B* **1988**, *38*, 807–813.

(60) Otero-de-la-Roza, A.; Johnson, E. R.; Luaña, V. CRITIC2: A Program for Real-Space Analysis of Quantum Chemical Interactions in Solids. *Comput. Phys. Commun.* **2014**, *185*, 1007–1018.

(61) de Gelder, R.; Wehrens, R.; Hageman, J. A. A Generalized Expression for the Similarity of Spectra: Application to Powder Diffraction Pattern Classification. *J. Comput. Chem.* **2001**, *22*, 273–289.

(62) Lacks, D. J.; Gordon, R. G. Pair Interactions of Rare-Gas Atoms as a Test of Exchange-Energy-Density Functionals in Regions of Large Density Gradients. *Phys. Rev. A* **1993**, *47*, 4681–4690.

(63) Zhang, Y.; Pan, W.; Yang, W. Describing van der Waals Interaction in Diatomic Molecules with Generalized Gradient Approximations: The Role of the Exchange Functional. *J. Chem. Phys.* **1997**, *107*, 7921–7925.

(64) Parrish, R. M.; Burns, L. A.; Smith, D.; Simmonett, A. C.; DePrince, A. E.; Hohenstein, E. G.; Bozkaya, U.; Sokolov, A. Y.; Di Remigio, R.; Richard, R. M. Psi4 1.1: An Open-Source Electronic Structure Program Emphasizing Automation, Advanced Libraries, and Interoperability. *J. Chem. Theory Comput.* **2017**, *13*, 3185–3197.

(65) Johnson, E. R.; Otero-de-la-Roza, A.; Dale, S. G.; DiLabio, G. A. Efficient Basis Sets for Non-Covalent Interactions in XDM-Corrected Density-Functional Theory. *J. Chem. Phys.* **2013**, *139*, 214109.

(66) Boys, S. F.; Bernardi, F. The Calculation of Small Molecular Interactions by the Differences of Separate Total Energies. Some Procedures with Reduced Errors. *Mol. Phys.* **1970**, *19*, 553–566.

(67) Mackie, I. A.; DiLabio, G. A. Approximations to Complete Basis Set-Extrapolated, Highly Correlated Non-Covalent Interaction Energies. *J. Chem. Phys.* **2011**, *135*, 134318.

(68) Björkman, T.; Gulans, A.; Krasheninnikov, A. V.; Nieminen, R. M. van der Waals Bonding in Layered Compounds from Advanced Density-Functional First-Principles Calculations. *Phys. Rev. Lett.* **2012**, *108*, 235502.

(69) Zacharia, R.; Ulbricht, H.; Hertel, T. Interlayer Cohesive Energy of Graphite from Thermal Desorption of Polyaromatic Hydrocarbons. *Phys. Rev. B* **2004**, *69*, 155406.

(70) Liu, H.; Neal, A. T.; Zhu, Z.; Luo, Z.; Xu, X.; Tománek, D.; Ye, P. D. Phosphorene: An Unexplored 2D Seminconductor with a High Hole Mobility. *ACS Nano* **2014**, *8*, 4033–4041.

(71) Kou, L.; Chen, C.; Smith, S. C. PhosphoreneL Fabrication, Properties, and Applications. *J. Phys. Chem. Lett.* **2015**, *6*, 2794–2805.

(72) Carvalho, A.; Wang, M.; Zhu, X.; Rodin, A. S.; Su, H.; Castro Neto, A. H. Phosphorene: From Theory to Applications. *Nat. Rev. Mater.* **2016**, *1*, 16061.

(73) Jing, Y.; Zhang, X.; Zhou, Z. Phosphorene: What Can We Know from Computations. *Wiley Interdiscip. Rev.: Comput. Mol. Sci.* **2016**, *6*, 5–19.

(74) Batmunkh, M.; Bat-Erdene, M.; Shapter, J. G. Phosphorene and Phosphorene-Based Materials – Prospects for Future Applications. *Adv. Mater.* **2016**, *28*, 8586–8617.

(75) Sansone, G.; Karttunen, A. J.; Usvyat, D.; Schutz, M.; Brandenburg, J. G.; Maschio, L. On the Exfoliation and Anisotropic Thermal Expansion of Black Phosphorus. *Chem. Commun.* **2018**, *54*, 9793–9796.

(76) Schulenburger, L.; Baczewski, A. D.; Zhu, Z.; Guan, J.; Tománek, D. The Nature of the Interlayer Interaction in Bulk and Few-Layer Phosphorus. *Nano Lett.* **2017**, *15*, 8170–8175.

(77) Sanone, G.; Maschio, L.; Usvyat, D.; Schutz, M.; Karttunen, A. Toward an Accurate Estimate of the Exfoliation Energy of Black Phosphorus: A Periodic Quantum Chemical Approach. *J. Phys. Chem. Lett.* **2016**, *7*, 131–136.

(78) Schutz, M.; Maschio, L.; Karttunen, A. J.; Usvyat, D. Exfoliation Energy of Black Phosphorus Revisited: A Coupled Cluster Benchmark. *J. Phys. Chem. Lett.* **2017**, *8*, 1290–1294.

(79) Brown, A.; Rundqvist, S. Refinement of the Crystal Strcuture of Black Phosphorus. *Acta. Cryst.* **1965**, *19*, 684–685.

(80) Schulenburger, L.; Mattson, T. R. Quantum Monte Carlo Applied to Solids. *Phys. Rev. B* **2013**, *88*, 245117.

(81) Mostaani, E.; Drummond, N. D. Quantum Monte Carlo Calculation of the Binding Energy of Bilayer Graphene. *Phys. Rev. Lett.* **2015**, *115*, 115501.

Graphical TOC Entry